Article

Oxidation of $Fe_{35}Mn_{21}Ni_{20}Cr_{12}Al_{12}$ High Entropy Alloy in Dry Air

Lamiaa Z. Mohamed [1],*[ID]**, Sanaa S. Abd ElMoamen** [2][ID]**, Seung Jo Yoo** [3] **and Mohamed Abdel-Hady Gepreel** [4],*[ID]

[1] Mining, Petroleum, and Metallurgical Engineering Department, Faculty of Engineering, Cairo University, Giza 12613, Egypt
[2] Tabbin Institute for Metallurgical Studies, Helwan 11421, Egypt
[3] Research Center for Materials Analysis, Korea Basic Science Institute (KBSI), Daejeon 34133, Republic of Korea; sjyoo78@kbsi.re.kr
[4] Materials Science and Engineering, Egypt-Japan University of Science and Technology (E-JUST), New Borg El-Arab City 21934, Egypt
* Correspondence: lamiaa.zaky@cu.edu.eg (L.Z.M.); mohamed.gepreel@ejust.edu.eg (M.A.-H.G.)

Abstract: The isothermal oxidation of a $Fe_{35}Mn_{21}Ni_{20}Cr_{12}Al_{12}$ high entropy alloy (HEA) was investigated in dry air for 50 h at 500, 600, and 700 °C after 90% cold rolling. The $Fe_{35}Mn_{21}Ni_{20}Cr_{12}Al_{12}$ HEA behaves according to the linear oxidation rate with rate constants of 1×10^{-6}, 3×10^{-6}, and 7×10^{-6} g/(cm^2·s) for oxidation at 500 °C, 600 °C, and 700 °C, respectively. The activation energy for oxidation of the HEA was calculated to be 60.866 KJ/mole in the 500–700 °C temperature range. The surface morphology and phase identification of the oxide layers were characterized. The formation of MnO_2, Mn_2O_3, Mn_3O_4, Cr_2O_3, and Al_2O_3 in the oxide layers along with Fe_2O_3 is the key to the oxidation mechanism. The elemental mapping and line EDX scans were performed to identify the oxidation mechanisms.

Keywords: high entropy alloys; cold rolling; oxidation; activation energy; surface morphology

1. Introduction

High entropy alloys (HEAs) are a new category of materials comprising more than five metallic elements ranging from 5–35 at. % [1–3]. The properties of HEAs are a unique combination of their metallic elements, such as high mechanical properties, good corrosion behavior, and wear and oxidation resistance [4–8]. Researchers have been concentrating on several factors, including composition design, fabrication procedures, and thermo-mechanical treatments, to improve the mechanical performance of HEAs by controlling microstructural features such as grain size and phases constitution. Grain boundaries function as obstacles to dislocation motion, successfully preventing dislocation motion. Thus, by adjusting the grain size, it is feasible to influence the shift of deformation mechanisms during deformation from dislocation slip to mechanical twinning. Thanks to improvements in processing techniques, achieving nanoscale grains is now a realistic aim that should increase the hardness or strength of HEAs [9]. Therefore, it is thought that cold rolling and annealing processes are a simple and very successful way to regulate HEAs' mechanical and microstructure characteristics while preserving their original composition [10]. According to reports, an increase in grain boundary density causes the oxide layer produced in fine grains to be more stable than that of coarse grains [10]. The diffusion rate of oxygen and metal atoms can be effectively reduced by severe lattice deformation, leading to a sluggish rate of oxide development [11].

HEAs have a little investigation of their oxidation mechanisms and behaviors in different media for industrial applications [12]. Annealing AlCrFeMnNi HEA improved its compressive strength and corrosion resistance [13,14]. The decrease or increase in the alloying elements compositions of HEAs leads to different structures with important influences on their properties. Thus, they are carefully chosen and added in controlled amounts [15,16]. The HEAs have the potential to be used in high-temperature environments.

However, studying the effect of different factors affecting the oxidation behavior of HEAs at different temperatures still needs much more work [17]. For example, including elements like Al, Si, and Cr may contribute to producing a stable protective oxide layer on the material surface at higher temperatures and improve oxidation resistance [18–20]. Many engineering components, including turbine blades, are covered by Al_2O_3 scales because the material is resilient across a broad temperature range even in harsh conditions like wet air or sulfidizing environments [20]. The Ni and Co elements are added as FCC stabilizers in Fe-rich HEAs [18,21]. The oxidation resistance of CoCrFeMnxNi HEA with low Mn (x = 0.51 wt.%) was excellent and close in behavior to 304H alloy at 650 °C and even better at 750 °C. The thin oxide layer scale formed at the CoCrFeNi surface was mainly Cr_2O_3, including some Mn oxides at the oxide/air interface. Increasing Mn content to x equals 20 wt.% in the same HEA leads to more rapid oxidation than low Mn one (especially at 750 °C) which may increase the possibility of oxide scale spallation. The high Mn HEA showed a thicker oxide scale which is Mn-rich at the oxide/air interface and Cr-rich close to the HEA/scale interface [22]. In some cases of HEAs oxidation behavior, it shows a parabolic kinetics nature but after some period instead of starting at time zero. Also, some cases show non-parabolic kinetics at the initial oxidation stages [23] because it needs time to form a protective oxide layer that works as a diffusion barrier and supports selective oxidation [22].

The behavior of HEAs under oxidation has much attention recently for investigation. Several issues are studied, including the effect of oxide-forming elements and the shear deformation on the oxide layer stability of HEAs. The amount of stable oxide-forming elements is the major factor affecting the HEAs' ability to withstand oxidation [24]. As a result, numerous research alter the concentration of stable oxide-forming components, particularly Al, to increase the oxidation resistance of HEAs [11]. The different alloying elements start to oxidize at different temperatures depending on their affinity as well as their evaporation partial pressure, for example, Mn > 300 °C, Al > 300 °C, Cr > 400 °C, Ni > 500 °C, and Fe > 700 °C are confirmed to oxidize [24]. Therefore, there is a greater chance that Mn and Al first produce oxide products. Certain fundamental information of multicomponent alloy that has been documented in previous work has shown that a transient oxidation state has been observed in the initial few hours before steady-state circumstances of oxidation. As a result of the first oxygen consumption, oxides, and other localized, non-uniform oxides have been detected during this brief interval. The following are potential oxidation orders: Mn → Al → Cr/Fe. As a result, at the beginning of the oxidation, oxidation behavior was changed [24]. Equimolar CrMnFeCoNi HEAs at 500–900 °C were also reported by Laplanche et al. Initially, liner behavior was seen throughout the oxidation process, but later, parabolic behavior was noted. Primarily α-Mn_2O_3, with a small layer of Cr_2O_3 (chromium) close to the edge where the oxide scale and HEA meet [24].

The plastic deformation produces a variety of microstructural characteristics, including high- and low-angle boundaries and a heterogeneous distribution of dislocations inside the material. In materials with high stacking fault energy, deformation may result in the formation of a tangled dislocation structure. Hence, a complex microstructure that influences the mechanical properties and strengthening mechanisms is produced by the deformation-induced substructures and the associated boundaries in the materials during deformation [25]. The deformation may be formed by a high density of accumulated dislocation and ultrafine/nano deformation twin bundles can hardly get a high work-hardening ability by weakened/suppressed activities of dislocation slip and twinning [26].

Reportedly, the cold-rolling technique worked well for fine-tuning the HEAs' grain structure. Most of these investigations concentrated on the changes in texture and microstructure that occurred during the annealing process of HEAs made by cold rolling [27]. The 90% reduction in thickness of the cold-rolled AlCoCrFeNi$_{2.1}$ HEA demonstrates a significant boost in strength. However, the investigation of a severe cold-rolled FeCoCrNiMn HEA with a reduction ratio greater than 90% has received very little attention [28].

The produced complex oxides of the HEAs cause slow oxidation kinetics, which could offer suitable intrinsic oxidation resistance for advanced applications. It is unclear; therefore, how compositional complexity and microstructure affect these alloys' oxidation processes [29]. $Fe_{35}Mn_{28}Ni_{20}Cr_{12}Al_5$ HEA was manufactured with FCC structure with good mechanical characteristics [30,31]. In addition, the oxidation behavior was examined in the air for 100 h at 900, 1000, and 1100 °C [1]. At this temperature range, it follows a parabolic rate law in oxidation with rate constants of 3.34×10^{-11}, 8.23×10^{-11}, and 1.42×10^{-10} $g^2/(cm^4 \cdot s)$ for 900 °C, 1000 °C, and 1100 °C, respectively, while the activation energy is 100.6 KJ/mol. In the present work, $Fe_{35}Mn_{21}Ni_{20}Cr_{12}Al_{12}$ HEA with (FCC + BCC) phase mixture is investigated. This new alloy has relatively higher strength than $Fe_{35}Mn_{28}Ni_{20}Cr_{12}Al_5$ and is still cold workable. The oxidation behavior of this new $Fe_{35}Mn_{21}Ni_{20}Cr_{12}Al_{12}$ HEA in the cold rolled condition is studied at the medium temperature range of 500, 600, and 700 °C for 50 h in dry air.

2. Experimental Work

$Fe_{35}Mn_{21}Ni_{20}Cr_{12}Al_{12}$ HEA was manufactured from pure elements using an arc melting furnace in an inert atmosphere and then cold rolled to a reduced thickness of 90% [3]. The cold rolled sheet was cut into $5 \times 5 \times 0.5$ mm^3 samples using a wire cutter. The basic roles of Al and Cr in this HEA are to stabilize the BCC phase, increase strength, decrease the oxidation rate, and increase the stability of the oxides more than the other present elements; Fe, Ni, and Mn [23,32]. The samples were ground from all surfaces with emery papers from 220 to 1000 grit, then polished with alumina paste 0.3 μm then cleaned with alcohol before oxidation. The phases formed were studied by X-ray diffractometer with the model (PRO PAN analytical diffractometer, X'Pert, Almelo, Netherlands) and the Cu Kα radiation source λ = 0.15406 nm, 45 V, and 40 mA with angles from 30 to 100. Transmission electron microscopy (TEM, JEM-ARM1300S, JEOL, Akishima, Japan) was used to characterize the phases of the alloy.

The oxidation experiments were conducted in dry air with a 2 lit/min flow rate at 500, 600, and 700 °C temperatures on the cold rolled specimens surfaces of the investigated HEA. To control the oxidation process, a vertical tube furnace (model EVA 12/300B, CARBOLITE GERO, Hope Valley, England) was used in conjunction with a program called "version programmer 3216 P5". The difference in weight of the oxidized HEAs in a 5h interval was monitored along the oxidation period by a high-accuracy electrical balance (Model MS 204 S/01, METTLER-TOLEDO, Greifensee, Switzerland) with an accuracy of 10^{-4} g. Scanning electron microscope (SEM, Quanta 250 FEG, FEI Company, Eindhoven, Netherlands) attached with energy dispersive X-ray analysis (EDX) was used to examine the surface morphology of the oxidized samples at 20 h and 50 h (Burker, AXS-flash detector 410 M, Leipzig, Germany). The oxidized HEAs cross-section at 50 h was prepared using mounting, then ground and polished to be characterized by SEM and line EDX across the oxide film.

3. Results

Figure 1 shows the structure of the present alloy and the phases constitution before the oxidation process. Figure 1a, and b are bright field (BF) TEM images and selected area diffraction (SAD) pattern images of the alloy, respectively, that show the alloy consists of FCC and BCC/B2 phases. This is confirmed in the XRD diffraction patterns shown in Figure 1c. Cold rolling is a common deformation method to produce metallic sheets for different applications. Cold rolling results in work hardening and some retained residual stress as well as possible texturing depending on the level of deformation [25]. The mechanical properties and detailed microstructure investigation of this alloy will be presented elsewhere. Below, we study the oxidation behavior of this new $Fe_{35}Mn_{21}Ni_{20}Cr_{12}Al_{12}$ HEA in the 90% cold rolled condition which is the working condition for some sheet metals at such a moderate temperature range.
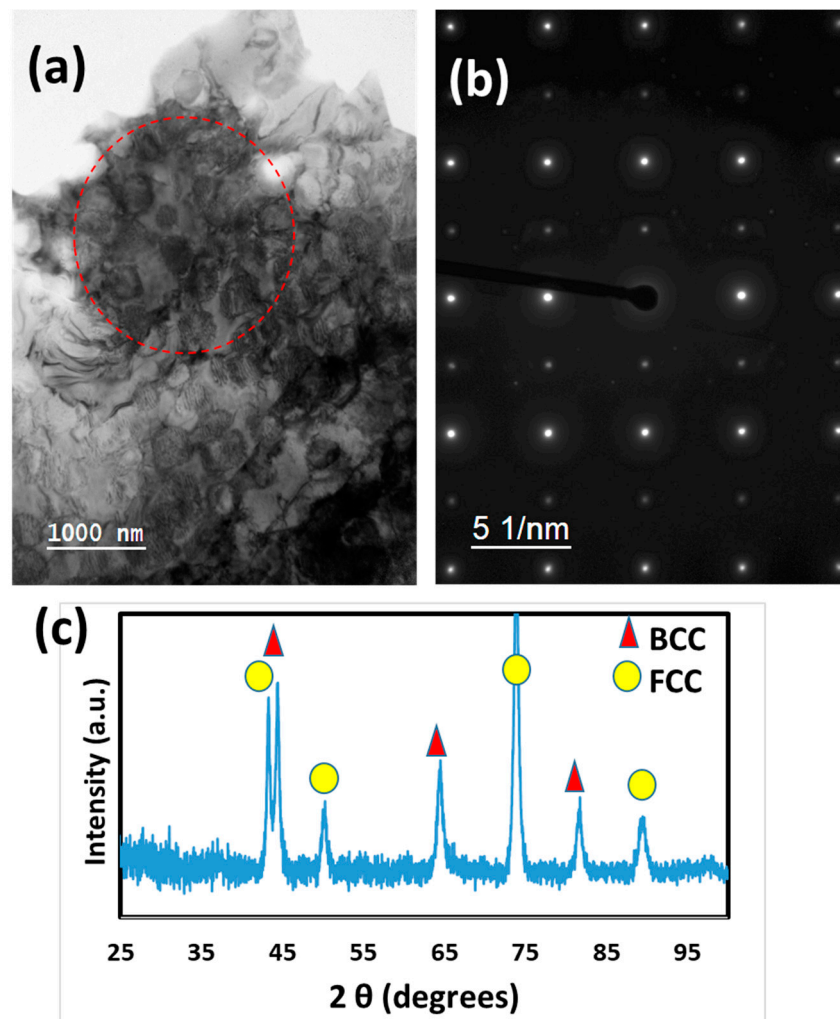
Figure 1. (**a**) BF TEM image with (**b**) the corresponding SAD pattern image in the red circle of a, and (**c**) XRD patterns of cold-rolled $Fe_{35}Mn_{21}Ni_{20}Cr_{12}Al_{12}$ HEA before oxidation.

3.1. Oxidation Kinetics

The weight change of the present HEA samples was recorded during the oxidation process, and then the weight gain was calculated. Here we consider only the oxidation process, so, dry air is considered to avoid complications if oxidation happens in humidified air [25]. Figure 2 illustrates the mass change/surface areas of tested samples during isothermal oxidation in dry air for 50 h at 500 °C, 600 °C, and 700 °C. Figure 2 shows the relation between the weight change vs. time which follows a linear relation, not parabolic. The oxidation kinetics of cold-rolled $Fe_{35}Mn_{21}Ni_{20}Cr_{12}Al_{12}$ HEA for 50 h at 600 and 700 °C follow the linear rate law. According to linear rate law Equation (1) [33] as presented in Figure 2, the oxidation rate exponent, n, nearly equals one, as reported in Table 1. The linear rate constant increases with increasing the oxidation temperature.

$$(\Delta W / \Delta A)^n = K_L \, t \qquad (1)$$

where t denotes the oxidation time, K_L denotes the linear rate constant, ΔW denotes the weight gain per unit area, n represents the rate exponent, and r represents the correlation coefficient.
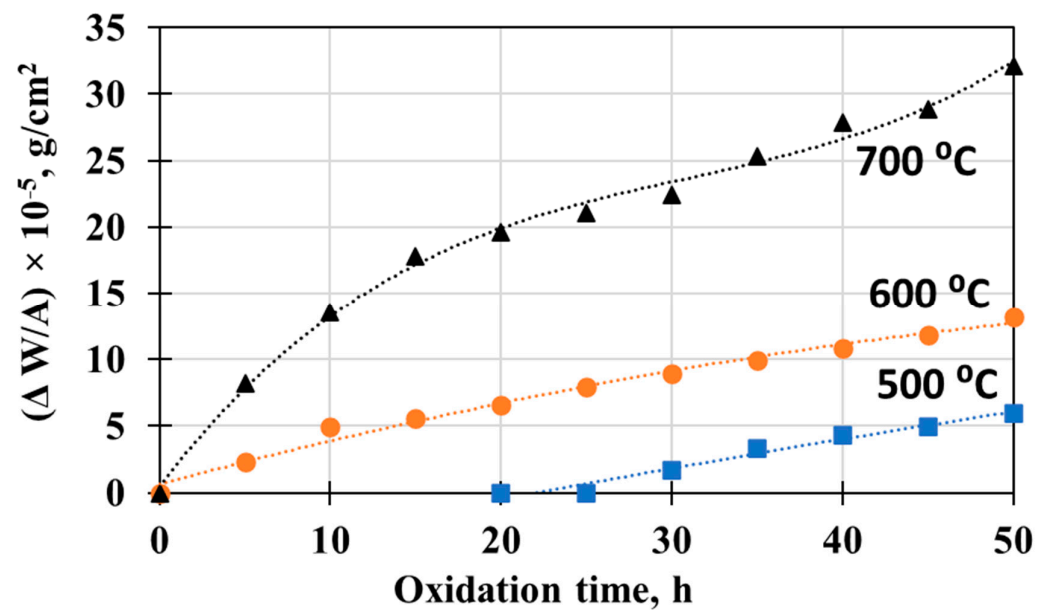
Figure 2. Weight gain ($\Delta W/A$) versus oxidation time of cold-rolled $Fe_{35}Mn_{21}Ni_{20}Cr_{12}Al_{12}$ HEA at 500, 600, and 700 °C in dry air for 50 h.

Table 1. The linear rate constant K_L of cold-rolled $Fe_{35}Mn_{21}Ni_{20}Cr_{12}Al_{12}$ HEA oxidized at 500, 600, and 700 °C in dry air for 50 h.

Temperature, °C	500	600	700
K_L, g/(cm²·s)	1×10^{-6}	3×10^{-6}	7×10^{-6}
r	0.9038	0.9608	0.903
n	1.00001	1.00004	1.00008

By applying the Arrhenius Equation (2), it could calculate the apparent activation energy of oxidation of the alloy as illustrated in Figure 3 [34,35].

$$K_L = A \exp(-Q/RT) \tag{2}$$

Figure 3. Variation of log k with $1/T$ of $Fe_{35}Mn_{21}Ni_{20}Cr_{12}Al_{12}$ HEA oxidation according to Arrhenius Equation (2).

R denotes the gas constant, Q represents the activation energy, T represents the oxidation temperatures in kelvin, and K_L represents the linear oxidation rate.

In comparison to the relevant system of $Fe_{35}Mn_{28}Ni_{20}Cr_{12}Al_5$ HEA, which has an activation energy of 100.6 kJ/mole in the temperature range between 900 °C and 1100 °C [1], the oxidation reaction of present HEA has a lower activation energy of 60.866 KJ/mole in the range of 500 °C to 700 °C. The activation energy in laboratory air in the temperature range of 650–750 °C for 1100 h for CoCrFeMnxNi with low Mn-content (x = 0.51 wt.%) is 162 KJ/mole, while by increasing Mn to 20.27 wt.% led to decreasing the activation energy to 111 KJ/mol [22]. Thus, a lower activation energy with a decrease in oxidation temperature range (500 °C to 700 °C) means the oxidation reaction occurs more readily at these temperatures due to the higher Al and lower Mn content. This alloy is in cold rolled condition (with high residual stresses) and with a duel phase BCC + FCC structure compared to the single FCC phase $Fe_{35}Mn_{28}Ni_{20}Cr_{12}Al_5$ alloy, thus, more factors activates oxidation process. The combined effect of Al and Mn in the HEA on the oxidation activation energy depends on their relative concentrations and interactions with other alloying elements along with the structure of the formed oxide layer. The oxidation behavior in HEAs is a complex phenomenon influenced by multiple factors; including the composition, microstructure, temperature, and the specific environment in which the oxidation takes place. It needs much investigation in the future to clearly understand these factors.

3.2. Phase Identification of Oxide Layer

The difficulty of distinguishing phases by XRD for HEAs may be due to their multicomponent/phase nature [22]. Peaks are overlapping for $MnFe_2O_3$ with those of Mn_3O_4, Fe_2NiO_4, Mn_2NiO_4, and Fe_3O_4. Also, Fe_2O_3 peaks overlap with Mn_2O_3 and $MnFeO_3$, or FeO from MnO or $Mn_{0.5}Fe_{0.5}O$ [22]. Figure 4 represents the XRD analyses of cold-rolled $Fe_{35}Mn_{21}Ni_{20}Cr_{12}Al_{12}$ HEA oxidized at 500, 600, and 700 °C in dry air for 50 h. The existing phases are mainly Fe_2O_3 (JCDPS 33-0644), MnO_2 (JCDPS 44-141), Mn_2O_3 (JCDPS 089-4836), Mn_3O_4 (JCDPS 02-0734), Cr_2O_3 (JCDPS 38-1479) and Al_2O_3 (JCPDS 46-1212). The iron/BCC phase (JCDPS 06-0696) appears at 500 °C only. It may be due to high oxidation resistance at 500 °C, resulting in a thin oxide layer; thus, the Fe/BCC phase appears in the XRD patterns. The low evaporation partial pressure and the high Mn content in this HEA (i.e., 21 at. %) resulted in different Mn-oxides appearing in the three oxidation temperatures and they are the main components of the oxide layer. It is clear that the angles of peaks are slightly shifted from their position which may be due to formation of spinel or complex phases due to the cocktail effect of the HEA formation. Those phases may be too small to be detected by XRD.
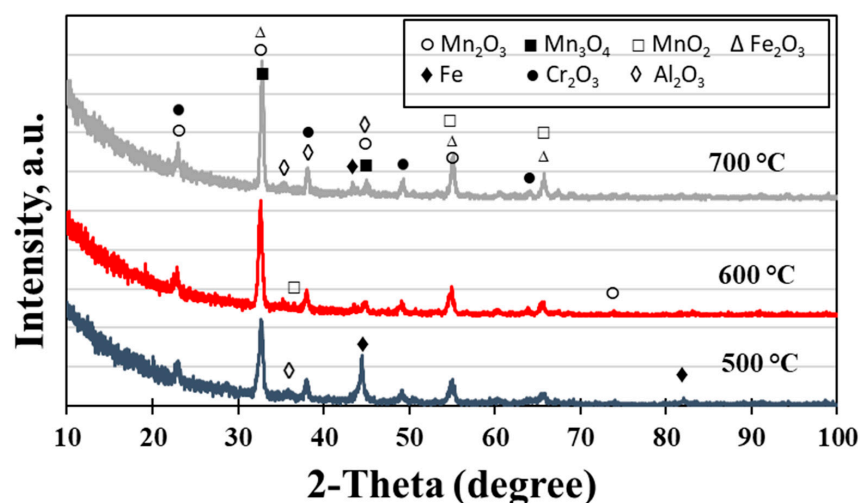

Figure 4. XRD patterns of cold-rolled $Fe_{35}Mn_{21}Ni_{20}Cr_{12}Al_{12}$ HEA oxidized at 500, 600, and 700 °C in dry air for 50 h.

3.3. Surface and Cross-Section Morphologies of the Oxide Layer

3.3.1. Oxidation at 500 °C

Figure 5 provides the SEM morphologies in the normal plane and the corresponding area analysis by EDX of the oxide layer after oxidation for 20 h and 50 h at 500 °C. The EDX analyses are given in Table 2. Increasing the oxidation time increases the manganese content on the surface of the oxide layer, which matches well with the line EDX scan results shown in Figure 6 along the cross-section. As shown in Figure 6, the oxide layer thickness is about 6 to 7 μm after 20 h and almost the same after 50 h. Figure 7 provides the EDX mapping of the elements after 50 h at 500 °C, which is in line with the previous investigation. The oxide layer contains mainly manganese oxides and iron oxide with small amounts of chromium oxides, and alumina.
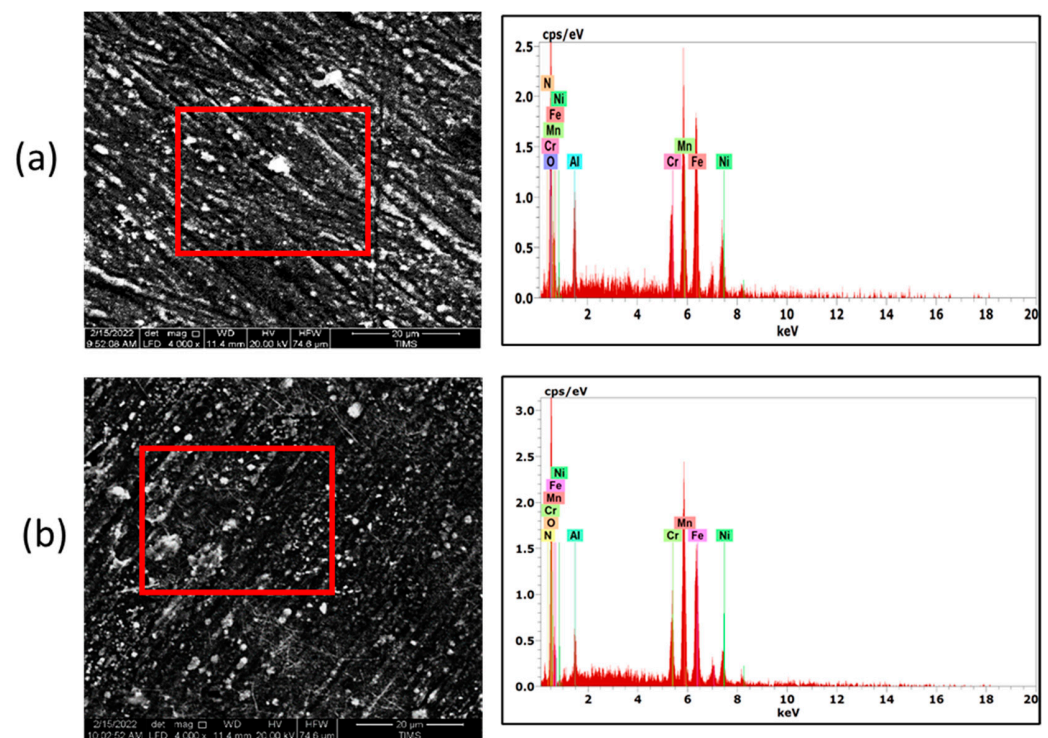

Figure 5. SEM images in the normal plane and corresponding EDX patterns of the surface of the alloy oxidized at 500 °C after (**a**) 20 h and (**b**) 50 h.

Table 2. The EDX analysis for the oxide surface at 500 °C at different oxidation times.

Conditions	Elements, at. %					
	O	**Fe**	**Mn**	**Ni**	**Cr**	**Al**
500 °C—20 h (Normal plane), Figure 5a	47.3	17.0	13.8	6.2	5.7	7.2
500 °C—50 h (Normal plane), Figure 5b	54.1	13.9	15.7	4.0	5.0	4.8
500 °C—50 h (CS, spot 1), Figure 6c	50.3	6.3	33.4	3.2	3.1	3.7
500 °C—50 h (CS, spot 2), Figure 6c	0.0	34.1	19.6	22.5	12.3	11.6

The protective Al_2O_3 typically forms on the air/oxide layer interface due to the high reactivity of aluminum with oxygen. The formation of the protective Cr_2O_3 can occur both on the air/oxide layer interface and within the oxide layer. The formation of manganese oxides in the investigated HEA can be more complex and they can form at various locations, including the air/oxide layer interface, oxide grain boundaries, or internal regions depending on the oxidation mechanisms involved.
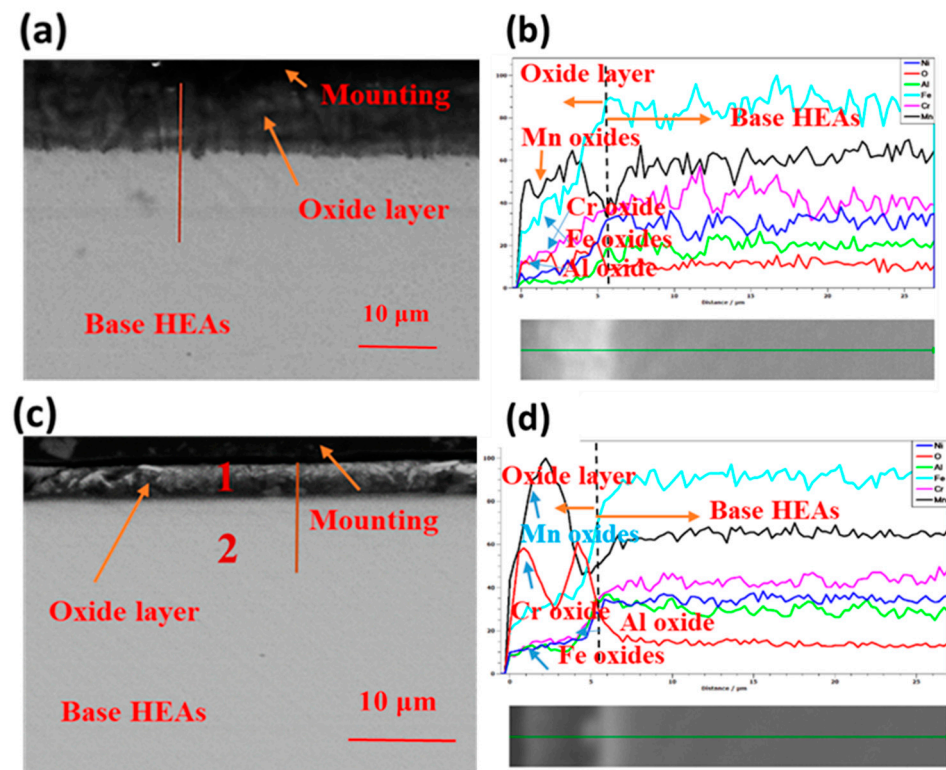
Figure 6. SEM images of the cross-section (CS) of the oxidized HEA at 500 °C for (**a**) 20 h and (**c**) 50 h and the corresponding Line–EDX analysis (**b**) and (**d**), respectively.
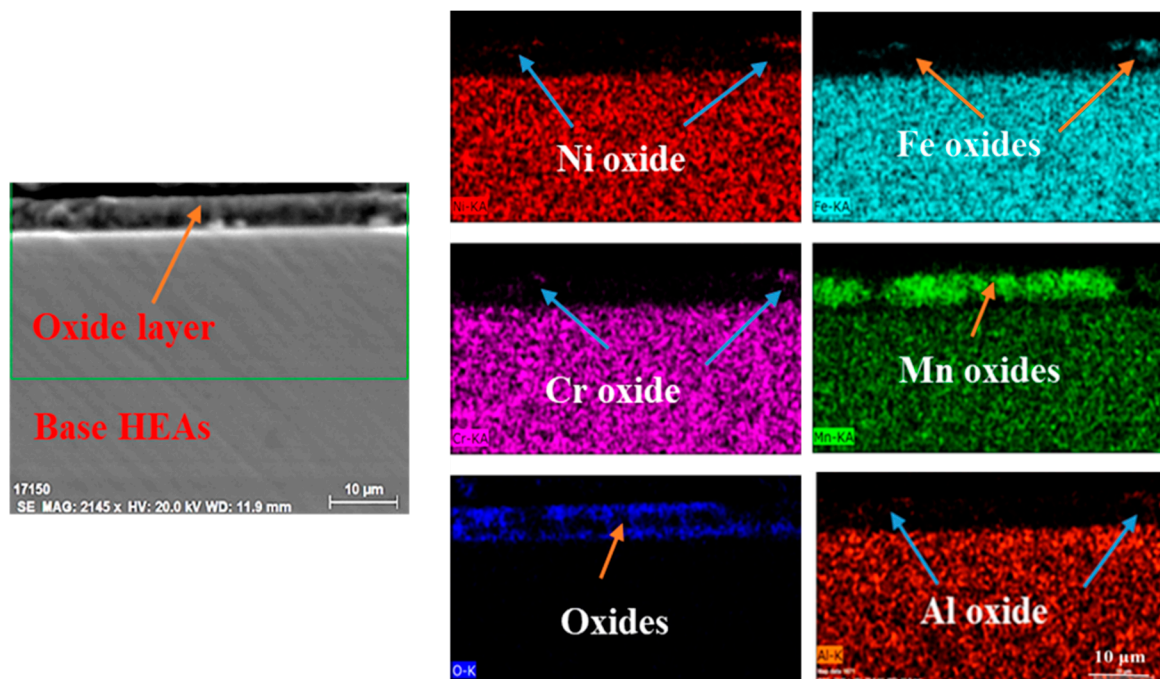

Figure 7. SEM/EDX cross-section elemental mapping of the oxide layer formed on the HEA after oxidation at 500 °C for 50 h.

3.3.2. Oxidation at 600 °C

Figure 8 shows the normal plane SEM images and the corresponding area analysis by EDX of the oxide layer after oxidation for 20 h and 50 h at 600 °C. The EDX results are

reported in Table 3. The oxide layer becomes coarser and more porous compared to the one formed at 500 °C. Increasing the oxidation time resulted in an increase in Al content on the air/oxide layer interface and much higher within the oxide layer, while manganese is almost the same. Figure 9 illustrates the line EDX analysis after 20 h that the manganese oxide is on the outer surface. After 50 h, the iron oxide layer with aluminum oxide under the manganese layer was reported. The oxide layer thickness is about 6 to 9 µm after 20 h oxidation while it is about 12 to 14 µm after 50 h. The EDX analyses of the cross-section for the oxide layer formed after 50 h at 600 °C are seen in Table 3, where Spot (3) is in the oxide layer and Spot (4) is in the base HEA. The increase in Al content in the interior of the oxide layer may be due to the formation of oxide precipitates [1]. Figure 10 demonstrates the cross-section mapping of the elements after 50 h at 600 °C, which aligns with the previous results. The elemental mapping shows the formation of duplex oxide layers that explain the seen layers in the line EDX analysis. Mn is well distributed among all oxide layers; however, the outer oxide layer is rich with Cr, Fe, and Al oxides.
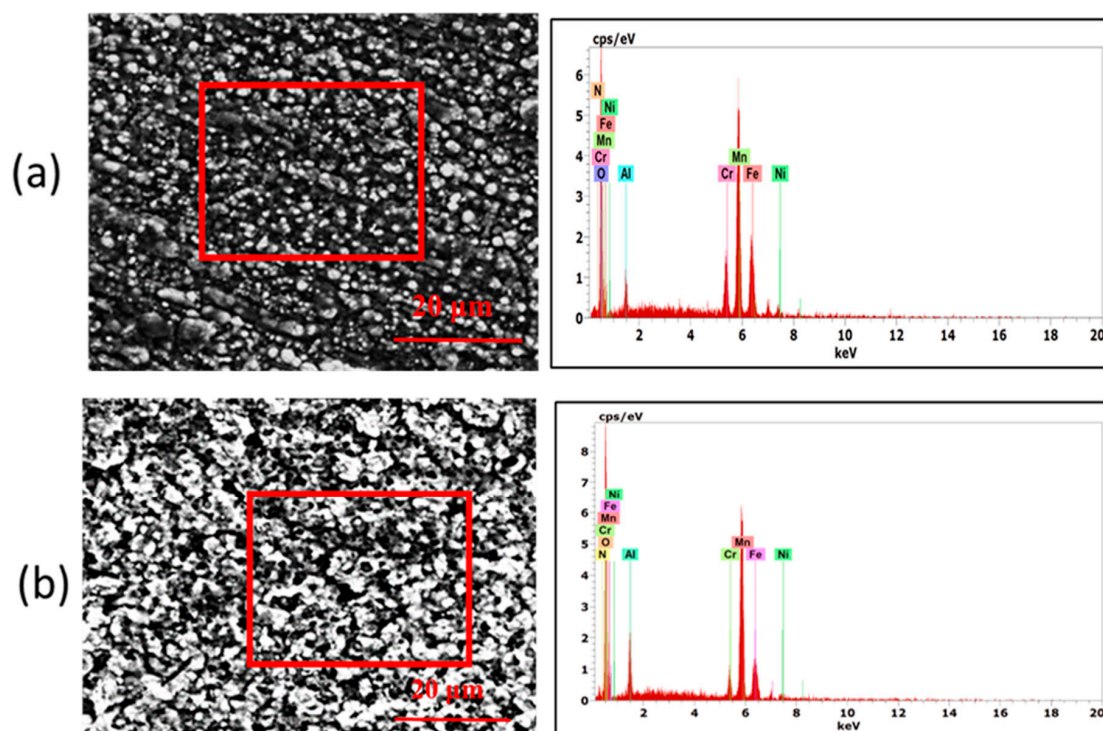

Figure 8. SEM morphologies and corresponding EDX patterns of the surface of alloy oxidized at 600 °C after (**a**) 20 h, and (**b**) 50 h.

Table 3. The EDX analysis for the oxide surface at 600 °C at different oxidation times and conditions.

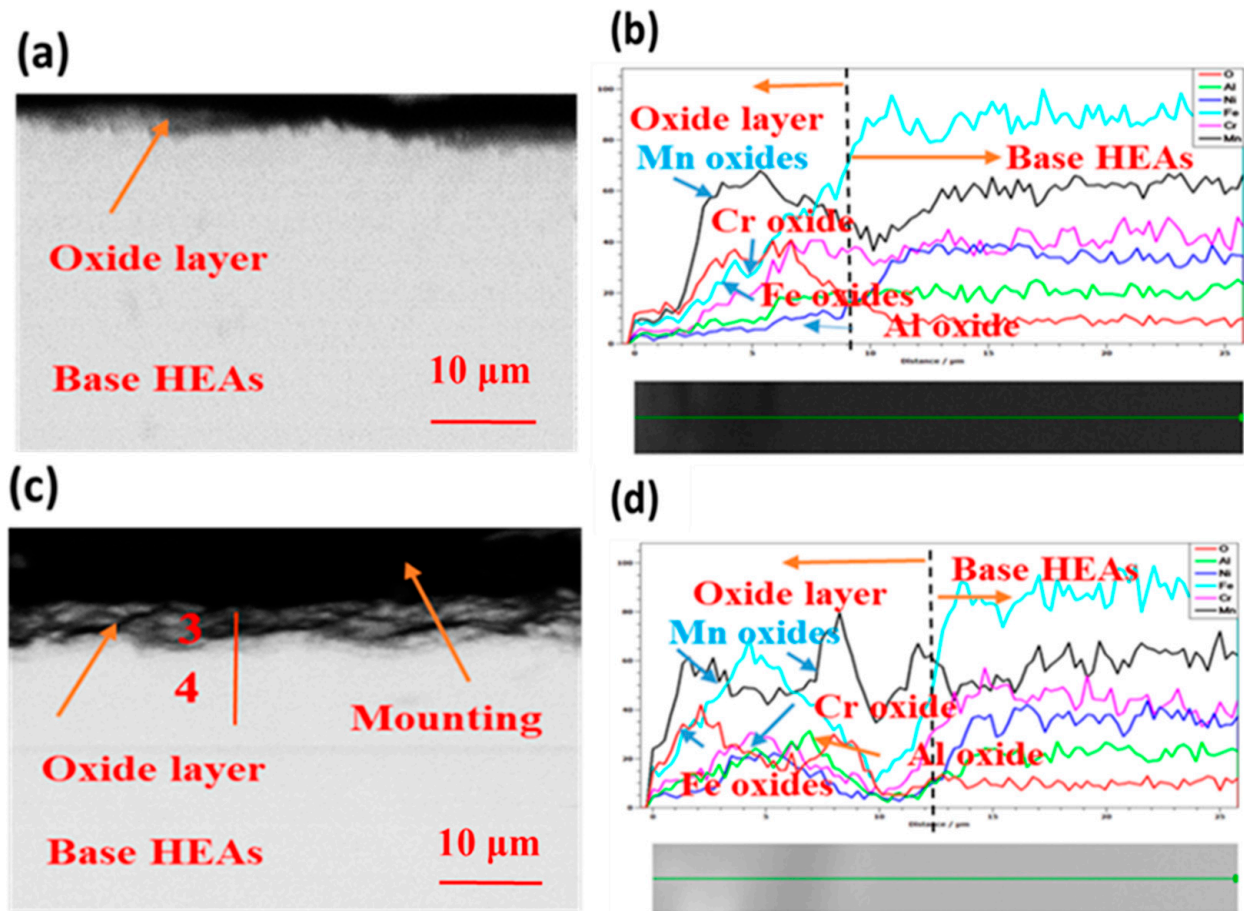| Conditions	Elements, at. %					
	O	Fe	Mn	Ni	Cr	Al
600 °C—20 h (Normal plane), Figure 8a	55.8	10.5	22.2	1.4	4.5	3.5
600 °C—50 h (Normal plane), Figure 8b	60.6	5.1	21.5	0.9	1.6	6.1
600 °C—50 h (CS, spot 3), Figure 9c	48.8	5.5	24.9	1.7	1.9	17.2
600 °C—50 h (CS, spot 4), Figure 9c	0.0	36.9	21.6	18.4	11.6	11.5

Figure 9. SEM images of the alloy cross-section of the oxidized at 600 °C for (**a**) 20 h and (**c**) 50 h and the corresponding Line–EDX analysis (**b**) and (**d**), respectively.
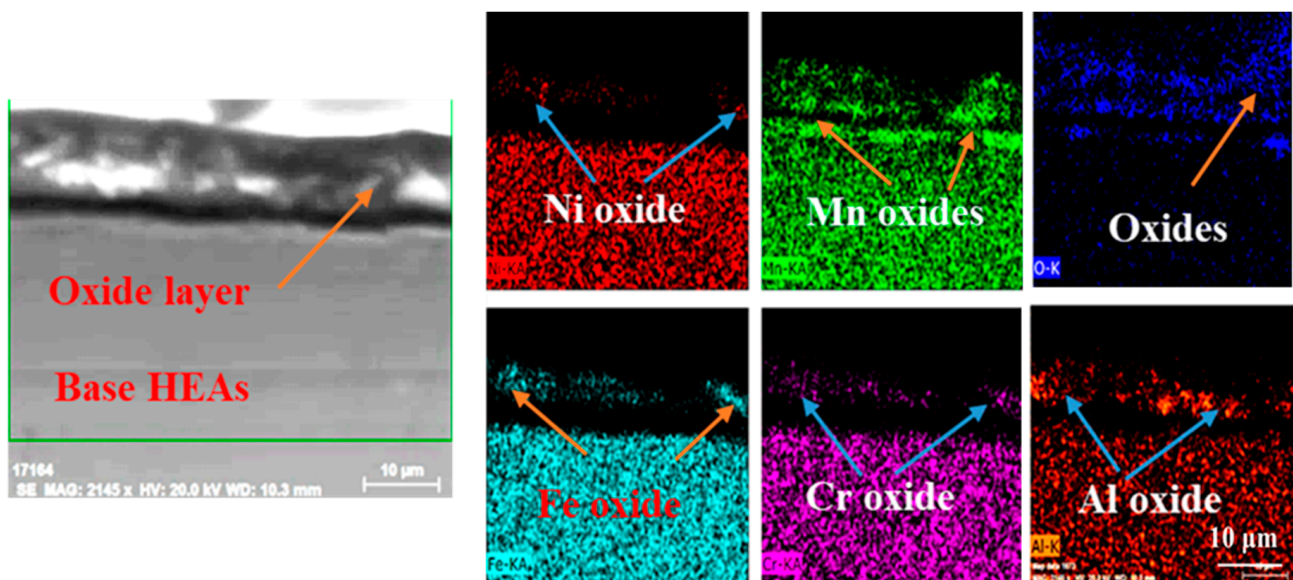

Figure 10. EDX mapping of the oxide layer formed on oxidized HEA at 600 °C for 50 h.

3.3.3. Oxidation at 700 °C

Figure 11 shows the SEM and EDX results of the oxide layer after oxidation at 700 °C for 20 h and 50 h. The oxide layer after 20 h seems much courser and porous than all other

conditions studied in the present work. The EDX analyses of the oxides are illustrated in Table 4. By increasing the oxidation time, both Mn, Al, and Fe content increase at the air/oxide interface. Figure 12 provides the cross-section and line EDX analyses after 20 h and 50 h. It shows a higher Mn and Fe on the outer surface (air/oxides interface) with a small content of aluminum oxide and chromium oxide. The oxide layer thickness is about 4 to 5 μm which is relatively thinner than other tested conditions and it is not a continuous layer after 50 h oxidation. This means there is a severe peel-off for the oxide layer formed at this oxidation temperature. Figure 13 gives the mapping of the elements after 50 h at 700 °C, which is in line with the previous investigation results. Elemental mapping in the cross-section proves the inhomogeneous thickness of the oxide layer. The oxide layer is rich with Mn, followed by Al, and small amounts of Cr and Ni oxides as precipitates.
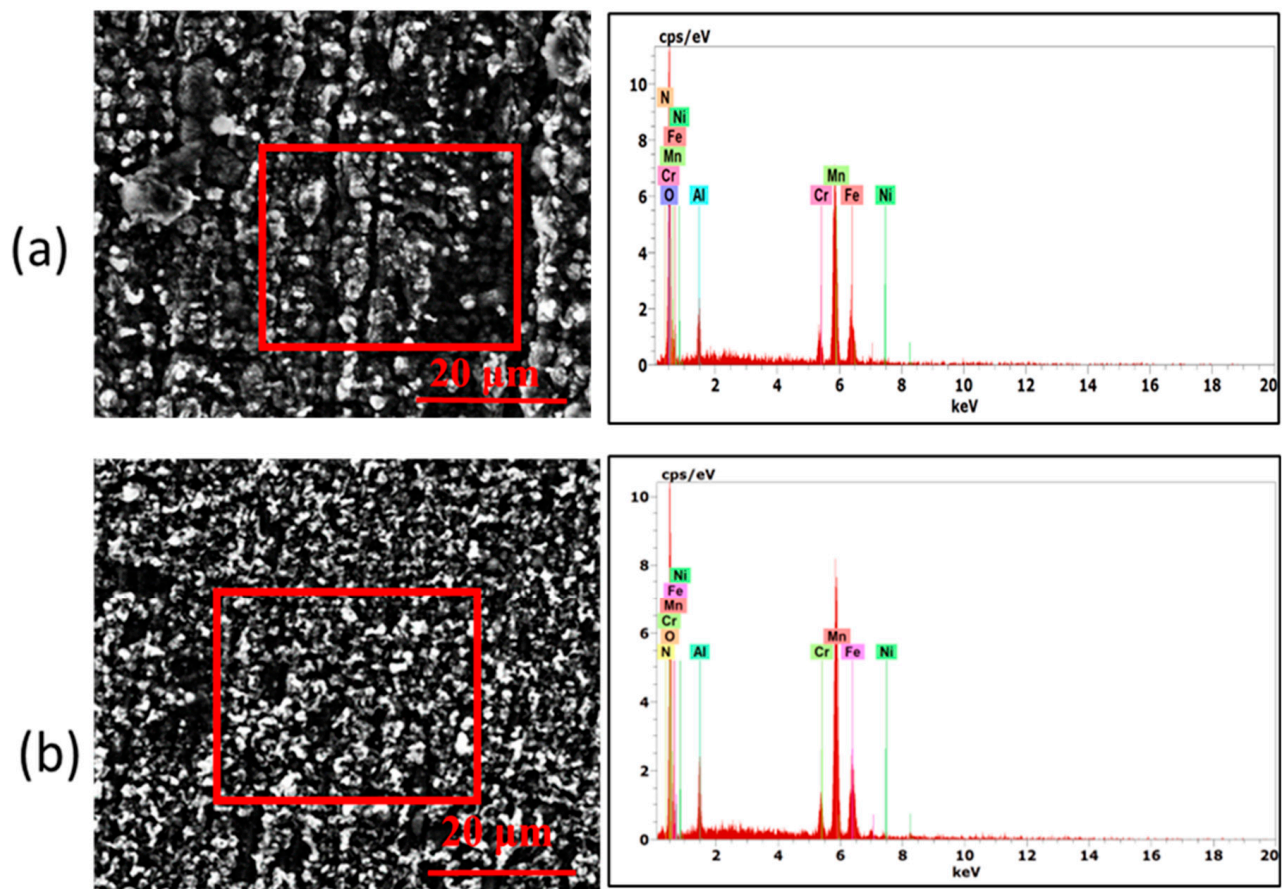

Figure 11. SEM micrographs and corresponding EDX patterns after oxidation at 700 °C for (**a**) 20 h and (**b**) 50 h.

Table 4. The EDX analysis for the oxide surface at 700 °C at different oxidation times and conditions.

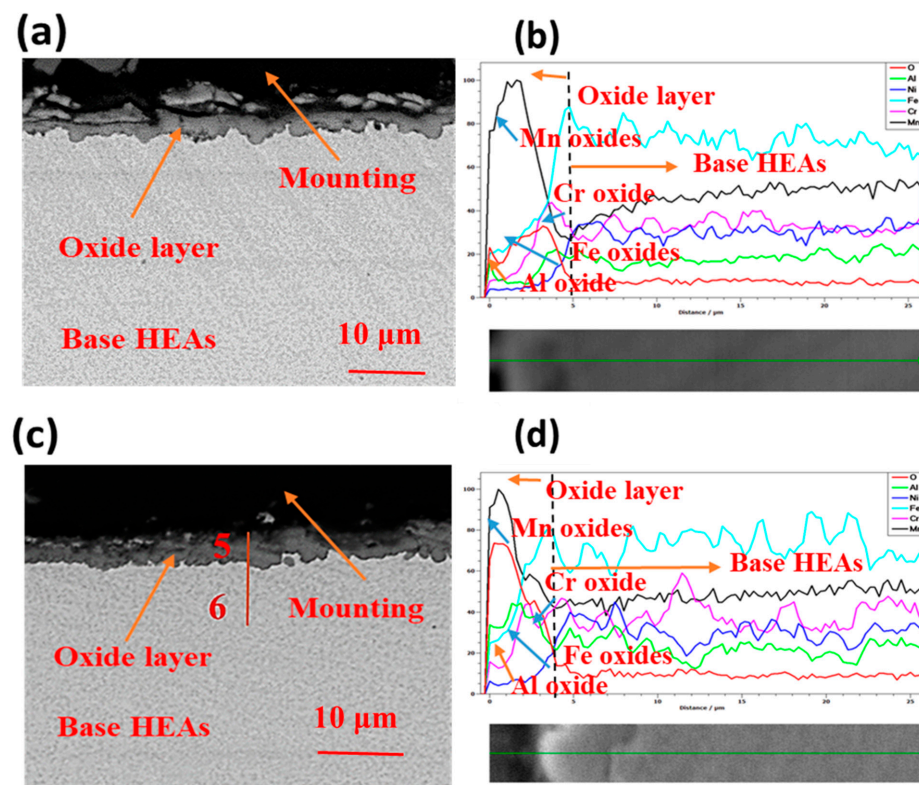| Conditions	Elements, at. %					
	O	Fe	Mn	Ni	Cr	Al
700 °C—20 h (Normal plane), Figure 11a	64.7	5.4	20.8	0.5	1.8	3.3
700 °C—50 h (Normal plane), Figure 11b	60.3	6.8	23.6	0.2	2.2	5.4
700 °C—50 h (CS, spot 5), Figure 12c	65.7	4.0	19.5	1.1	2.9	6.8
700 °C—50 h (CS, spot 6), Figure 12c	0.0	32.7	18.3	24.9	12.0	12.1

Figure 12. SEM images of the alloy cross-section of the oxidized at 700 °C for (**a**) 20 h and (**c**) 50 h and the corresponding Line–EDX analysis (**b**) and (**d**), respectively.
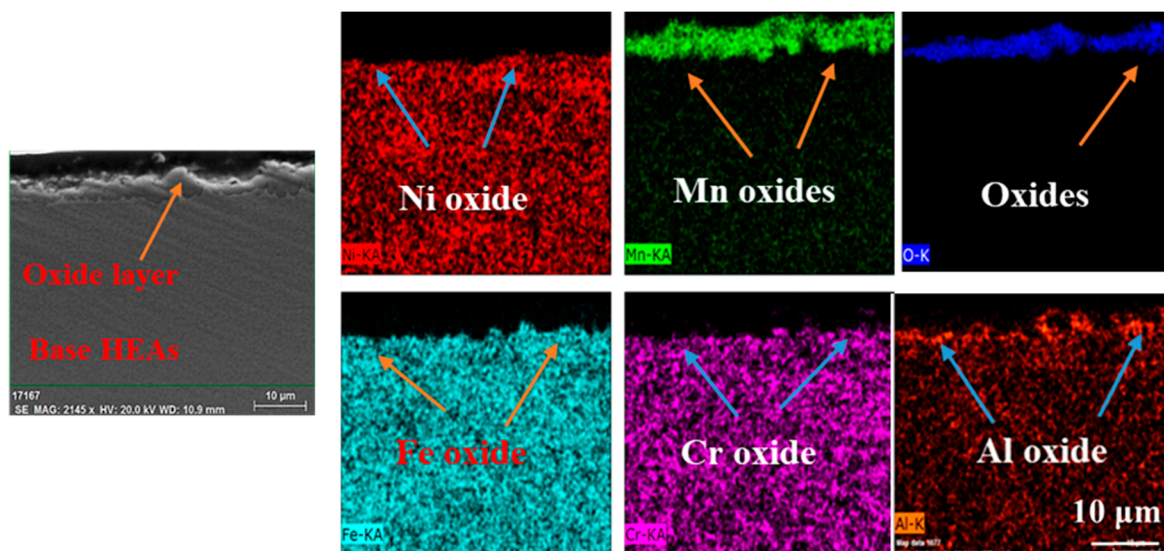

Figure 13. Mapping of the oxide layer formed on oxidized HEA at 700 °C for 50 h.

4. Discussion

The oxide layers formed in the different investigated temperatures are porous and not continuous may be because the oxidation temperatures are lower than that needed to contain a continuous protective layer by Al_2O_3 [23,32]. Also, the continuous spallation of the formed layer results in a small amount of Al in the oxide layer as reported in Tables 2–4 [36,37]. Since Mn has considerably higher mobility in the spinel than Cr or Fe elements, the Mn oxide often is found rich in the outer layer reducing the protection effect

of other formed Al and Cr oxides [38]. However, the significance of Mn in the oxidation mechanism of such HEAs is still not completely understood [39]. Due to the formation of Mn-enrichment spinel in the oxide layer, Mn is used as a stabilizer of the austenite phase in austenitic steels, which impacts the oxidation resistance. Mn diffusion slows down with oxidation time due to the drop in Mn near the oxide/metal boundary caused by the shift of Mn from metal to oxide film. As a result, the diffusion mechanism cannot regulate the pace of total oxidation [17]. High-entropy MnCoCrFeNi alloy has an oxidation activation energy of 130 kJ/mol [17,40], which is lower than the activation energy of diffusion of Mn in HEA (288 kJ/mol) [8]. However, it is still higher than the diffusion of Mn in Mn oxides (122 kJ/mol) [17]. Therefore, the rate-limiting process is the Mn diffusion through the oxide [8].

In the present study, $Fe_{35}Mn_{23}Ni_{20}Cr_{12}Al_{12}$ HEA has about 60% of the activation energy for oxidation at 500–700 °C range compared to the same HEA system with lower Al content oxidized at 900–1100 °C ($Fe_{35}Mn_{28}Ni_{20}Cr_{12}Al_5$) [1]. In the present oxidation case, the high thermal stresses that resulted from sample cooling and thermal shock may be the cause of the low spallation resistance [41]. In addition to this, the common oxide/metal interface cracking is caused by a mismatch in the thermal expansion coefficients of the oxide scale and bulk material that still occurs. Also, the present alloy is in the cold rolled condition which means high internal stresses and high dislocation density are present that reduce the oxidation resistance and produce non-protective oxide layers (i.e., the oxide layers do not contain/maintain protective layers). This may be the main reason the investigated HEAs follow the linear not parabolic oxidation rate. The Mn content is about twice the Al content in this HEA, thus, the Mn oxides are noticed after the Fe oxides. The linear oxidation rate of the HEA means the oxide layers are non-protective and may be cracked or loose from the outer surfaces. Due to the Pilling-Bedworth Ratio (PB Ratio), the non-protective layers have a PB ratio less than unity. This may be due to the difference in the oxide layers formed on the investigated HEA as given in Figure 4. The XRD patterns and EDX analysis indicated the existence of Al, Cr, Fe, and Mn oxides in almost all conditions.

The SEM images of the oxide scales after 50 h at 500, 600, and 700 °C indicate the homogeneity of the layers formed with spallation in some parts of the oxide layer and the formation of the duplex layer at 600 °C. Normally, the formation of protective layers may be explained by the parabolic oxidation behavior of the alloy [35], which is not the case for the present alloy at the investigated temperature range. The oxide layer thickness increases with the increase in the oxidation temperatures from 500 °C to 600 °C. By increasing the temperature to 700 °C the cracks appear and part of the oxide layer falls down and the thickness decreases as confirmed in Figure 12. This is the reason for the linear oxidation rate behavior of the HEA. Due to the HEA composition complexity, the oxidation mechanism at this temperature is inwardly controlled by oxygen. Generally, the formation of Al_2O_3 and Cr_2O_3 protective layers decreases the inward diffusion of oxygen through the air/scale interface [42]. Mn outward diffusion is higher than Cr by ~2 orders of magnitude and their oxides have high vacancies which permit the oxygen to diffuse inwardly [43]. The high manganese content in the oxide layer proposes that the oxidation mechanism is done by the outward diffusion mechanism. Almost all the formed oxide layers formed at different conditions contain Mn (mainly), Al, and a smaller content of Cr, Fe, and Ni oxides. Spinel structures may be formed in the oxide layers such as $MnCr_2O_4$ and $MnFe_2O_4$ formation, however, it is not identified by XRD due to the small amount that may be formed.

There is limited knowledge about the high-temperature oxidation behaviors and mechanisms of HEAs. Most research on HEAs focuses on comprehending the idea of design, forming, phases formation, properties determination, and control as well as advanced production, characterization, and applications. The limited studies conducted on the oxidation behaviors of HEAs have given, in most cases, only partial insights into the kinetics or microstructural details of the oxide scale [1]. Therefore, it is highly needed to go further in studying the mechanism of oxidation in HEAs under different conditions and compositions.

5. Conclusions

The oxidation behavior of 90% cold-rolled $Fe_{35}Mn_{21}Ni_{20}Cr_{12}Al_{12}$ HEA at 500, 600, and 700 °C in dry air for 50 h has been investigated. This study's findings are summarized as follows:

1. The oxidation kinetics of HEA are obeying the linear rate law. The linear rate constants at 500 °C, 600 °C, and 700 °C are 1×10^{-6}, 3×10^{-6}, and 7×10^{-6} g/(cm^2·s), respectively.
2. The oxidation activation energy is calculated to be 60.866 KJ/mol at the 500–700 °C temperature range.
3. The oxide layer contains manganese oxides (main phases), iron oxide, aluminum oxide, and chromium oxide at 600 and 700 °C, along with a few iron phase observed at 500 °C.
4. The duplex oxide layer of Fe, Mn Al, and Cr oxides appears at 600 and 700 °C. The oxide layer thickness increases with increasing the oxidation temperature from 500 to 600 °C. By increasing to 700 °C, the oxide layer cracked and spelled out part of them thus the oxide layers thickness decreased.
5. The oxidation mechanism at 500 and 600 °C is proposed to be an outward diffusion of Al, Cr, and Mn and an inward diffusion of O. However, for oxidation at 700 °C, it seems the inward diffusion of O is more dominant due to the high vacancy concentration in the formed Mn-rich oxide layer. 700 °C, the inward diffusion of oxygen through the vacancies of the rich Mn oxides is more active.

References

1. Ali, M.M.; Abd ElMoamen, S.S.; Gepreel, M.A.H.; Ahmed, H.A.; Elrefaie, F.A. High temperature oxidation of non equi-atomic Al5Cr12Fe35Mn28Ni20 high entropy alloy. *Mater. Res. Express* **2021**, *8*, 036508. [CrossRef]
2. Gaber, G.A.; Abolkassem, S.A.; Elkady, O.A.; Tash, M.; Mohamed, L.Z. ANOVA and DOE of comparative studies of Cu/Mn effect on corrosion features of CoCrFeNi high entropy alloy immersed in different acidic media. *Chem. Paper* **2022**, *2*, 1675–1690. [CrossRef]
3. Mohamed, L.Z.; Gepreel, M.A.H.; Abdelfatah, A. Corrosion behavior of Al12Cr12Fe35Mn21Ni20 high entropy alloy in different acidic media. *Chem. Pap.* **2021**, *75*, 6265–6274. [CrossRef]
4. Miracle, D.B.; Miller, J.D.; Senkov, O.N.; Woodward, C.; Uchic, M.D.; Tiley, J. Exploration and Development of High Entropy Alloys for Structural Applications. *Entropy* **2014**, *16*, 494–525. [CrossRef]
5. Senkov, O.N.; Senkova, S.V.; Woodward, C.; Miracle, D.B. Low-density, refractory multi-principal element alloys of the Cr–Nb–Ti–V–Zr system: Microstructure and phase analysis. *Acta Mater.* **2013**, *61*, 1545–1557. [CrossRef]
6. Senkov, O.N.; Senkova, S.V.; Woodward, C. Effect of aluminum on the microstructure and properties of two refractory high-entropy alloys. *Acta Mater.* **2014**, *68*, 214–228. [CrossRef]

7. Gludovatz, B.; Hohenwarter, A.; Catoor, D.; Chang, E.H.; George, E.P.; Ritchie, R.O. A fracture-resistant high-entropy alloy for cryogenic applications. *Science* **2014**, *345*, 1153–1158. [CrossRef]

8. Laplanche, G.; Volkert, U.F.; Eggeler, G.; George, E.P. Oxidation Behavior of the CrMnFeCoNi High-Entropy Alloy. *Oxid. Met.* **2016**, *85*, 629–645. [CrossRef]

9. Deng, W.; Xing, S.; Chen, M. Effect of annealing treatments on microstructure, tensile and wear properties of cold-rolled FeCoCrNiMn high entropy alloy. *J. Mater. Res. Technol.* **2023**, *27*, 3849–3859. [CrossRef]

10. Abdelghany, A.W.; Jaskari, M.; Hamada, A.S.; Gepreel, M.A.H.; Järvenpää, A. Study on the Deformation Mechanism of a Nonequiatomic AlCrMnFeNi High-Entropy Alloy at Cold and Warm Temperatures. *Solid State Phenom.* **2023**, *353*, 19–24. [CrossRef]

11. Shao, Y.; Guo, P.; Liang, N.; Cheng, S.; Wang, J.; Xu, F. Microstructure refinement and enhanced mechanical properties in rapid-quenched MnCrFeCoNi high-entropy alloy. *Heliyon* **2023**, *9*, e22530. [CrossRef] [PubMed]

12. Yan, G.; Zheng, M.; Gu, J.; Li, C. High-temperature oxidation behavior of laser additively manufactured AlCrCoNiSi-based high-entropy alloys at 1100 °C. *J. Alloys Compd.* **2023**, *976*, 173120. [CrossRef]

13. Huang, P.K.; Yeh, J.W.; Shun, T.T.; Chen, S.K. Multi-Principal-Element Alloys with Improved Oxidation and Wear Resistance for Thermal Spray Coating. *Adv. Eng. Mater.* **2004**, *6*, 74–78. [CrossRef]

14. Mohamed, L.Z.; Elsayed, A.H.; Elkady, O.A.; Abolkassem, S.A. Physico-mechanical, microstructure, and chemical properties of Si/Ti/Nb additions to CoCrMoW medium entropy alloys. *J. Mater. Res. Technol.* **2023**, *24*, 9897–9914. [CrossRef]

15. Dąbrowa1, J.; Cieślak, G.; Stygar, M.; Zajusz, M.; Jawańska, M.; Gil1, A.; Jedliński, J.; Mroczka, K.; Matsuda, K.; Kulik, T.; et al. Oxidation Behavior of Alx(CoCrFeNi)100-x High-Entropy Alloys Under Thermal-Cycling Conditions. *Oxid. Met.* **2021**, *96*, 307–321. [CrossRef]

16. Oluru, M.T.; Mitrica, D.; Soare, V.; Constantin, I.; Burada, M.; Dumitrescu, D.; Caragea, A.; Carlan, B.A.; Banica, C.I.; Stoiciu, F.; et al. Synthesis and characterization of high entropy alloys for high temperature applications. *UPB. Sci. Bull. Series B* **2019**, *81*, 249–256.

17. Ren, X.; Li, Y.; Qi, Y.; Wang, B. Review on Preparation Technology and Properties of Refractory High Entropy Alloys. *Materials* **2022**, *15*, 2931. [CrossRef]

18. Veselkov, S.; Samoilova, O.; Shaburova, N.; Trofimov, E. High-Temperature Oxidation of High-Entropic Alloys: A Review. *Materials* **2021**, *14*, 2595. [CrossRef]

19. Anne, B.R.; Shaik, S.; Tanaka, M.; Basu, A. A crucial review on recent updates of oxidation behavior in high entropy alloys. *SN Appl. Sci.* **2021**, *3*, 366. [CrossRef]

20. Ouyang, D.; Chen, Z.-J.; Yu, H.-B.; Chan, K.; Liu, L. Oxidation behavior of the Ti38V15Nb23Hf24 refractory high-entropy alloy at elevated temperatures. *Corros. Sci.* **2022**, *198*, 110153. [CrossRef]

21. Gorr, B.; Müller, F.; Schellert, S.; Christ, H.-J.; Chen, H.; Kauffmann, A.; Heilmaier, M. A new strategy to intrinsically protect refractory metal based alloys at ultra-high temperatures. *Corros. Sci.* **2020**, *166*, 1084. [CrossRef]

22. Ogura, M.; Fukushima, T.; Zeller, R.; Dederichs, P.H. Structure of the high-entropy alloy AlxCrFeCoNi: FCC versus BCC. *J. Alloys Compd.* **2017**, *715*, 454–459. [CrossRef]

23. Aniołek, K.; Kupka, M.; Łuczuk, M.; Barylski, A. Isothermal oxidation of Ti–6Al–7Nb alloy Vacuum 114 114–8 10. *Mater. Res. Express* **2015**, *8*, 036508.

24. Kofstad, P. *High Temperature Corrosion*; Elsevier Applied Science Publishing: London, UK, 1988.

25. Dewangan, S.K.; Kumar, D.; Kumar, V.; Ahn, B. Surface oxidation behavior of spark plasma sintered AlCrCuFeMnWx high entropy alloys at an elevated isothermal temperature. *Int. J. Refract. Met. Hard Mater.* **2024**, *119*, 106531. [CrossRef]

26. Safyari, M.; Hojo, T.; Moshtaghi, M. Effect of environmental relative humidity on hydrogen-induced mechanical degradation in an Al–Zn–Mg–Cu alloy. *Vacuum* **2021**, *192*, 110489. [CrossRef]

27. Abdelghany, A.W.; Jaskari, M.; Hamada, A.S.; Järvenpää, A.; El-Hofy, H.A.; Chiba, A.; Gepreel, M.A.-H. Hot deformation behavior and constitutive modeling of a cost-effective Al8Cr12Mn25Ni20Fe35 high-entropy alloy. *J. Alloy. Compd.* **2022**, *928*, 167028. [CrossRef]

28. Li, Z.; Fu, L.; Zheng, H.; Yu, R.; Lv, L.; Sun, Y.; Dong, X.; Shan, A. Effect of Annealing Temperature on Microstructure and Mechanical Properties of a Severe Cold-Rolled FeCoCrNiMn High-Entropy Alloy. *Met. Mater. Trans. A* **2019**, *50*, 3223–3237. [CrossRef]

29. Mahmoud, E.R.; Shaharoun, A.; Gepreel, M.A.; Ebied, S. Studying the Effect of Cold Rolling and Heat Treatment on the Microstructure and Mechanical Properties of the Fe36Mn20Ni20Cr16Al5Si3 High Entropy Alloy. *Entropy* **2022**, *24*, 1040. [CrossRef]

30. Butler, T.M.; Senkov, O.N.; Daboiku, T.I.; Velez, M.A.; Schroader, H.E.; Ware, L.G.; Titus, M.S. Oxidation behaviors of CrNb, CrNbTi, and CrNbTaTi concentrated refractory alloys. *Intermetallics* **2022**, *140*, 107374. [CrossRef]

31. Elkatatny, S.; Gepreel, M.A.H.; Hamada, A. Effect of Cold Rolling on the Microstructure and Hardness of Al5Cr12Fe35Mn28Ni20 High Entropy Alloy. *Mater. Sci. Forum* **2018**, *917*, 241–245. [CrossRef]

32. Elkatatny, S.; Gepreel, M.A.; Hamada, A.; Nakamura, K.; Yamanaka, K.; Chiba, A. Effect of Al content and cold rolling on the microstructure and mechanical properties of Al5Cr12Fe35Mn28Ni20 high-entropy alloy. *Mater. Sci. Eng. A* **2019**, *759*, 380–390. [CrossRef]

33. Young, D.J. *High Temperature Oxidation and Corrosion of Metals*, 2nd ed.; Elsevier: Oxford, UK, 2016.

34. Mohamed, L.Z.; Abd Elmomen, S.; El-Hadad, S. Investigating the thermal oxidation behavior of Ti–6Al–7Nb alloy in dry air. *Mater. Corro.* **2022**, *73*, 1553–1562. [CrossRef]

35. Mohamed, L.Z.; Abd Elmomen, S.; El-Hadad, S. Influence of the oxidation behavior of Ti–6Al–4V alloy in dry air on the oxide layer microstructure. *Chem Paper.* **2022**, *76*, 1627. [CrossRef]

36. Castaldi, L.; Kurapov, D.; Reiter, A.; Shkover, V.; Schwaller, P.; Patscheider, J. High temperature phase changes and oxidation behavior of Cr–Si–N coatings. *Surf. Coat. Technol.* **2007**, *202*, 781–785. [CrossRef]

37. Okamoto, H.M.-O. Manganese-Oxygen. *J. Phase Equilibria Diffus.* **2007**, *28*, 307. [CrossRef]

38. Wood, G.C. High-temperature oxidation of alloys. *Oxid. Met.* **1970**, *2*, 11–57. [CrossRef]

39. Holcomb, G.R.; Tylczak, J.; Carney, C. Oxidation of CoCrFeMnNi High Entropy Alloys. *JOM J. Miner. Met. Mater. Soc.* **2015**, *67*, 2326–2339. [CrossRef]

40. Han, J.; Li, X.; Gerard, A.Y.; Lu, P.; Saal, J.E.; Frankel, G.S.; Ogle, K.; Scully, J.R. Potential Dependent Mn Oxidation and Its Role in Passivation of Ni38Fe20Cr22Mn10Co10 Multi-Principal Element Alloy Using MultiElement Resolved Atomic Emission Spectroelectro chemistry. *J. Electrochem. Soc.* **2021**, *168*, 051508. [CrossRef]

41. Zhang, Y.; Zuo, T.T.; Tang, Z.; Gao, M.C.; Dahmen, K.A.; Liaw, P.K.; Lu, Z.P. Microstructures and properties of high-entropy alloys. *Prog. Mater. Sci.* **2014**, *61*, 1–93. [CrossRef]

42. Korda, A.A.; Akbar, M.A.; Muhammad, F.; Achmad, T.L.; Prawara, B.; Prajitno, D.H.; Jihad, B.H.; Setianto, M.H.; Basuki, E.A. High-Temperature Oxidation and Microstructural Changes of Al0.75CoCrFeNi High-Entropy Alloy at 900 and 1100 °C. *Metals* **2024**, *14*, 33. [CrossRef]

43. White, E.M.H.; Bürckner, M.-L.; Schlereth, C.; Bik, M.; Galetz, M.C. High-Temperature Oxidation Behavior of FeCoCrNi+(Cu/Al)-Based High-Entropy Alloys in Humid Air. *Crystals* **2024**, *14*, 60. [CrossRef]